Atomically Thin, Ionic Covalent Organic Nanosheets for Stable, High-Performance Carbon Dioxide Electroreduction

Yun Song, Jun-jie Zhang, Yubing Dou, Zhaohua Zhu, Jianjun Su, Libei Huang, Weihua Guo, Xiaohu Cao, Le Cheng, Zonglong Zhu, Zhenhua Zhang, Xiaoyan Zhong, Dengtao Yang, Zhaoyu Wang, Ben Zhong Tang, Boris I. Yakobson*, Ruquan Ye**

Y. Song, Y. Dou, Z.-H. Zhu, J. Su, L. Huang, W. Guo, X. Cao, L. Cheng, Prof. Z.-L. Zhu, Prof. R. Ye

Department of Chemistry and State Key Laboratory of Marine Pollution, Hong Kong Institute for Advanced Study, City University of Hong Kong, Hong Kong 999077, China

E-mail: ruquanye@cityu.edu.hk

Prof. R. Ye

City University of Hong Kong Shenzhen Research Institute, Shenzhen 518057, China

Prof. X. Zhong

Department of Materials Science and Engineering, City University of Hong Kong, Hong Kong 999077, China

Prof. D.-T. Yang

School of Chemistry and Chemical Engineering, Northwestern Polytechnical University, Xi'an 710072, China

E-mail: dtyang@nwpu.edu.cn

This is the author manuscript accepted for publication and has undergone full peer review but has not been through the copyediting, typesetting, pagination and proofreading process, which may lead to differences between this version and the Version of Record. Please cite this article as doi: 10.1002/adma.202110496.

Z. Wang, Prof. B. Z. Tang

School of Science and Engineering, Shenzhen Institute of Molecular Aggregate Science and Technology, The Chinese University of Hong Kong, Shenzhen, Guangdong 518172, China

Dr. J.-J. Zhang, Prof. B. I. Yakobson

Department of Materials Science and Nanoengineering, Rice University, Houston, Texas 77005, USA

E-mail: biy@rice.edu

Z. Zhang

Institute of Advanced Magnetic Materials, College of Materials and Environmental Engineering, Hangzhou Dianzi University, Hangzhou 310012, China; Shenzhen Futian Research Institute, City University of Hong Kong, Shenzhen 518048, China

Department of Chemistry

Rice University

6100 Main Street , Houston , TX 77005 , USA

Department of Chemistry

Rice University

6100 Main Street , Houston , TX 77005 , USA

Keywords: carbon dioxide reduction, ultrathin, ionic nanosheets, covalent organic frameworks, positively charged

Abstract: The incorporation of charged functional groups is effective to modulate the activity of molecular complexes for CO_2 reduction reaction (CO_2RR), yet the long-term heterogeneous electrolysis is often hampered due to catalysts leaching. Herein, for the first time, an electrocatalyst of atomically thin, cobalt porphyrin-based, ionic covalent organic nanosheets (CoTAP-iCONs) is synthesized via a post-synthetic modification strategy for high-performance CO_2-to-CO conversion.

The cationic quaternary ammonium groups not only enable the formation of monolayer nanosheets due to steric hindrance and electrostatic repulsion, but also facilitate the formation of *COOH intermediate as suggested by theoretical calculations. Consequently, CoTAP-iCONs exhibit higher CO_2RR activity than other cobalt porphyrin-based structures: an 870% and 480% improvement of CO current densities compared to the monomer and neutral nanosheets, respectively. Additionally, the iCONs structure can accommodate the cationic moieties. In a flow cell, CoTAP-iCONs attain a very small onset overpotential of 40 mV and a stable total current density of 212 mA cm^{-2} with CO Faradaic efficiency of >95% at -0.6 V for 11 h. Further coupling the flow electrolyzer with commercial solar cells yields a solar-to-CO conversion efficiency of 13.89%. This work indicates that atom-thin, ionic nanosheet is a promising structure for achieving both tailored activity and high stability.

1. Introduction

Electrochemical CO_2 reduction reaction (CO_2RR) is a promising method to convert renewable electricity into high-value products and mitigate industrial CO_2 emissions [1-7]. However, the thermodynamic stability of CO_2[8,9] and the competing hydrogen evolution reaction (HER)[10] impede the practical application and commercialization of CO_2RR process. Recently, great efforts have been dedicated to developing various homogeneous and heterogeneous electrocatalysts for effective and selective reduction of CO_2 to CO. Homogeneous molecular catalysts[11-21], such as metalloporphyrins and metallophthalocyanines, can be systematically optimized by switching metal centers[15] and tailoring ligand structures[10,11,14,16,19,21] to achieve high selectivity. Over the past decades, molecular catalysts with cationic functional groups have been shown to exhibit much higher catalytic activity than their neutral counterparts[17,22-26]. For example, iron porphyrin with four trimethylammonium groups at the ortho positions of phenyl groups exhibited a significant decrease of the catalytic overpotential while dramatically increase of the turnover frequency (TOF)[22]. However, ionic molecular catalysts are water-soluble[24,27]. When the catalyst is directly coated on the electrode surface, many of the ionic molecules will leach from the electrode, which hampers their long-term stability[28,29].

In recent years, various methods have been developed to immobilize molecular catalysts, including non-covalent π-π interaction[17,30], direct metal-to-substrate coordination[31,32], and covalent grafting at peripheral functional groups[33,34]. For instance, Hu et al. reported a heterogeneous catalyst by immobilizing cobalt meso-tetraphenylporphyrin onto carbon nanotubes (CoTPP-CNT) through π-π interaction[35]. The resultant CoTPP-CNT composite shows a current density of 0.59 mA cm^{-2} with 83% CO selectivity at an overpotential of 350 mV, which was much better than the homogeneous process in dimethylformamide. Even though some of the heterogeneous catalysts exhibit high-performance electrochemical CO_2RR[36,37], conventional immobilization methods cannot accommodate the ionic molecular catalysts at the electrode due to their high water solubility. The construction of stable ionic molecular catalysts/electrode interfaces to achieve both high stability and activity remains challenging.

The integration of molecular catalytic units into extended frameworks, such as covalent triazine frameworks (CTFs)[38-40], covalent organic frameworks (COFs)[41-43] and conjugated microporous polymers (CMPs)[44-46], has attracted attention for electrocatalytic CO_2 reduction reaction because of their advantageous electronic and structural properties. First, the spatial arrangement of well-defined molecular active sites into covalently connected networks ensures excellent catalytic activity and stability. Second, the high porosity and expanded conjugated structure facilitate mass transport and electron transfer. Third, the electronic characteristic of molecular active sites can be further modulated by functional linker. However, most of the porous organic polymers are π-π stacked layer structures, which limit the accessibility of adsorbates to active sites and have poor electron conductivity, thereby inevitably impeding their electrocatalysis performance.

In contrast, ultrathin structure endows catalysts with attractive properties, including large surface area, highly exposed electrocatalytic active sites, rapid mass transport, and superior electron transfer[47-50]. Therefore, the use of ultrathin two-dimensional (2D) covalent organic nanosheets is an effective strategy to improve electrochemical activity. Various synthetic methods[51-53] have been applied to fabricate ultrathin covalent organic nanosheets. Among them, incorporating charged units into the skeleton of ionic covalent organic nanosheets (iCONs)[51,54-56] can be utilized to introduce electrostatic repulsive interaction between layers and assist the self-exfoliation of nanosheets.

In this work, we report the synthesis of ultrathin, ionic, cobalt porphyrin-based covalent organic nanosheets (CoTAP-iCONs), and the first reported example of ionic frameworks for efficient and stable CO_2 electroreduction. We adopted a post-synthetic modification process for the synthesis; as recently reported by the Adronov's[57] groups, the successful decoration of ammonium and iminium groups between COF layers (COF-DIBO-N^+Me_3) weakens the interlayer stacking interaction. Analogous introduction of ionic groups in the framework of CoTAP-iCONs helps the exfoliation into nanosheets with an average thickness of ~0.5 nm. This atomically thin structure vastly exposes the cobalt active sites, which improves the turnover frequency of CO (TOF_{CO}). More importantly, the confinement of catalytic moiety in the framework resolves the common leaching problem of ionic catalysts. Density functional theory (DFT) calculations further reveal that the quaternary ammonium cations decrease the energy barrier for the formation of *COOH, which is the rate-determining step for CO_2RR. The advantage of the ultrathin and ionic structure is exemplified by the CO_2RR activity. CoTAP-iCONs exhibit high CO selectivity of 96.74% with a partial current density of 11.92 mA cm^{-2} at -0.65 V in an H-type cell, which is ~870% and 480% higher than that of monomeric cobalt porphyrin (CoTAP) and neutral cobalt porphyrin-based nanosheets (CoTAP-CONs)

under similar cobalt loadings, respectively. To demonstrate the industrial application potential, we apply CoTAP-iCONs in a flow cell that reaches a partial current density of 300.2 mA cm^{-2} at -0.75 V, outperforming most of the reported cobalt-based electrocatalysts. We further demonstrate a solar-driven electrochemical CO_2 reduction device. The solar-driven flow cell achieves a solar-to-CO conversion efficiency of 13.89% with CO Faradaic efficiency of 94.83% at an average current density of 21.87 mA cm^{-2} for 12 h. This work presents an efficient cobalt porphyrin-based electrocatalyst for solar-driven CO_2 reduction reaction and provides a strategy to construct ionic ultrathin nanosheets.

2. Results and Discussion

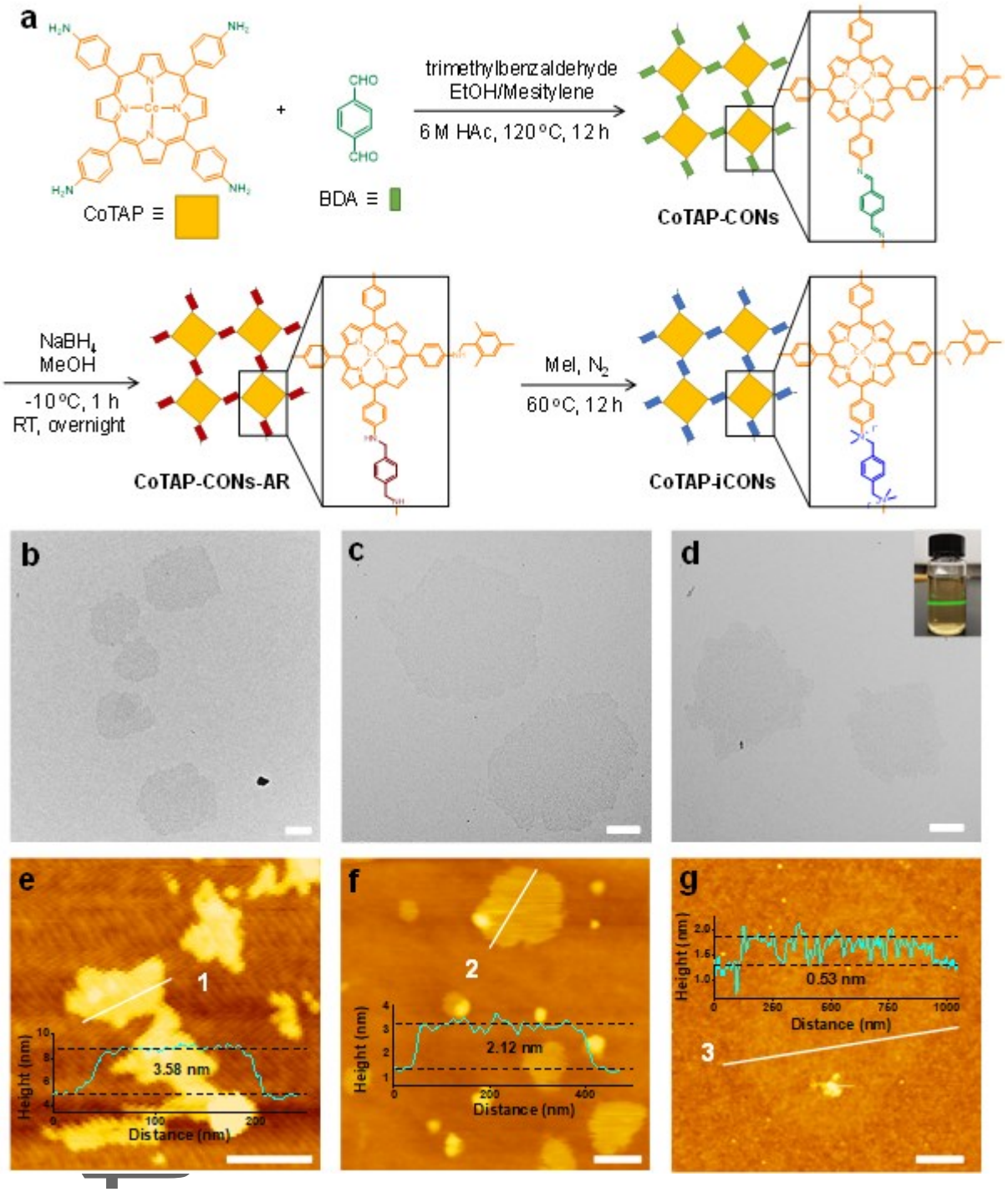

Figure 1. a) Schematic illustration for the synthesis of CoTAP-iCONs. TEM and AFM images of CoTAP-CONs (b,e), CoTAP-CONs-AR (c,f), and CoTAP-iCONs (d,g). Scale bar: 200 nm.

CoTAP-iCONs were synthesized following the scheme in **Figure 1**a. First, thin-layer CoTAP-CONs with bulky 2,4,6-trimethylphenyl groups on the edge were prepared by condensation reaction[58]. Then, CoTAP-CONs-AR were prepared by reducing the imine bond of CoTAP-CONs using sodium borohydride. Lastly, the amine group was methylated to obtain CoTAP-iCONs modified with quaternary ammonium groups. The morphologies of the as-obtained samples are characterized by transmission electron microscopy (TEM) and atomic force microscopy (AFM). Figures 1b,e show that CoTAP-CONs present few-layer nanosheet morphology with a lateral size of several hundred nanometers and a thickness of ~3 nm. The corresponding energy-dispersive X-ray spectroscopy (EDS) element mapping analysis reveals that C, N, and Co elements are uniformly distributed throughout the architecture of CoTAP-CONs (Figure S1). In the case of CoTAP-CONs-AR, similar two-dimensional nanosheets are observed and the thickness slightly reduces to ~2 nm (Figure 1c,f). The individual transparent nanosheets of CoTAP-iCONs are shown in Figure 1d with EDS mapping in Figure S2. There is no significant morphological change after methylation, suggesting that the structure is well preserved. The Tyndall effect in the inserted picture confirms the colloid properties of CoTAP-iCONs suspension. Due to the high electron beam sensitivity of ultrathin covalent organic nanosheets[59-62], CoTAP-iCONs rapidly deteriorate under a high accelerating voltage and it is difficult to directly measure lattice fringes. To solve this problem, we reduce the amount of bulky group agents and methylation agents to synthesize CoTAP-iCONs in larger size (Figure S3), and investigate the interlayer spacing. Figure S3b shows an interlayer spacing of 0.43 nm in short-range ordering of nanodomains. CoTAP-iCONs are further characterized by AFM. The measurement height of CoTAP-iCONs decreases to 0.53 nm, which roughly corresponds to the thickness of a monolayer nanosheet, while the width is retained at several hundred nanometers (Figure 1g). More AFM data of CoTAP-

iCONs are shown in Figure S4, and the results detected in different regions indicate that the thickness of CoTAP-iCONs ranges from 0.55 to 0.62 nm. The powder X-ray diffraction (pXRD; Figure 2a) data show the amorphous polymeric nature of CoTAP-iCONs. The poor structural periodicity could be attributed to the bulky functional groups, which is similar to the recently reported COF-DIBO-C_8[57]. The CoTAP-iCONs powder exhibits a broad diffraction peak at 2θ=21.09°, which corresponds to a spacing of 0.42 nm calculated from Bragg's equation (**Figure 2**a). Therefore, the incorporation of methylated ammonium groups into the skeleton disturbs the interlayer stacking and facilitates the formation of ultrathin nanosheets via electrostatic repulsion and steric hindrance.

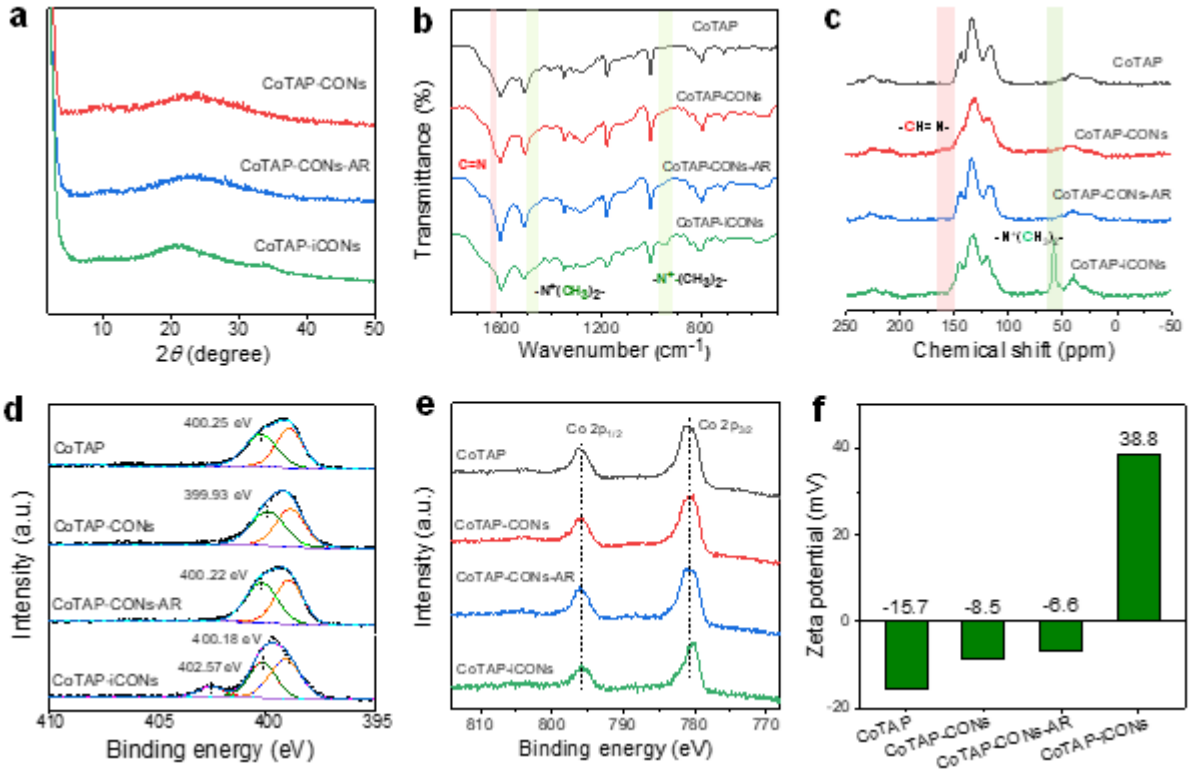

Figure 2. (a) pXRD spectra of CoTAP-CONs, CoTAP-CONs-AR, and CoTAP-iCONs, (b) FT-IR spectra, (c) ^{13}C solid-state NMR spectra, (d) N 1s XPS spectra, (e) Co 2p XPS spectra, and (f) Zeta potential of CoTAP, CoTAP-CONs, CoTAP-CONs-AR, and CoTAP-iCONs.

The chemical structure of CoTAP-iCONs is further verified by Fourier transform infrared (FT-IR) spectroscopy, solid-state ^{13}C solid-state nuclear magnetic resonance (^{13}C NMR) and X-ray photoelectron spectroscopy (XPS). For CoTAP-CONs, Figure 2b shows the characteristic C=N stretching vibrational bands at 1619 cm^{-1}, indicating the successful formation of imine bond in CoTAP-CONs structure. After reduction, the imine vibrational bands are not detected, which suggests the complete conversion of CoTAP-CONs to CoTAP-CONs-AR. Furthermore, new vibrational peaks at 956 and 1480 cm^{-1} represent the new C-N stretching and -CH_3 bending vibration of -N^+-$(CH_3)_2$- groups in the framework of CoTAP-iCONs. Analogous phenomena are also observed in solid-state ^{13}C NMR spectra. All three modified samples show similar resonance signals at 111.8, 117.2, 134.3, 144.4, and 151.2 ppm, confirming the preservation of porphyrin units in the network[63,64] (Figure 2c). CoTAP-CONs show a unique peak at 160 ppm, which is assigned to the carbon atom of C=N bond. The disappearance of imine carbon peak of CoTAP-CONs-AR further confirms the successful reduction process. The newly formed amine carbon peak is located at 51 ppm, but it overlaps with the sideband. Notably, CoTAP-iCONs exhibit a new peak belonging to methyl groups at 58 ppm, which is consistent with the FT-IR results.

XPS tests are conducted to explore the surface electronic state and elemental composition of covalent organic nanosheets. Two high-resolution N 1s peaks at 399.93 and 398.88 are ascribed to C=N and Co-N_4 structure in CoTAP-CONs. The resultant CoTAP-iCONs display binding energy peaks at 402.57, 400.18 and 399.24 eV, corresponding to quaternary ammonium nitrogen atoms (10.9%),

amine nitrogen atoms (37.6%) and Co-N_4 (51.5%), which indicates that ~25% of the amine groups are turned into quaternary ammonium groups. The Co 2p spectra show the valence state of coordinated cobalt atoms. The binding energies of Co $2p_{3/2}$ and Co $2p_{1/2}$ for CoTAP-CONs are 780.79 and 796.08 eV, which are respectively blue-shifted to 780.35 and 795.73 eV for CoTAP-iCONs due to the electron-withdrawing effect of methylated ammonium groups[65] (Figure 2e). Moreover, the cobalt content of CoTAP, CoTAP-CONs, CoTAP-CONs-AR and CoTAP-iCON are determined to be 6.5, 5.1, 4.9 and 4.1 wt% by ICP analyses, respectively. The positively charged network of CoTAP-iCONs is further verified by zeta potential analysis in Figure 2f (detailed distribution curves in Figure S5). The ethanol suspensions of CoTAP, CoTAP-CONs, CoTAP-CONs-AR, and CoTAP-iCONs show a zeta potential of -15.7, -8.5, -6.6 and 38.8 mV, respectively.

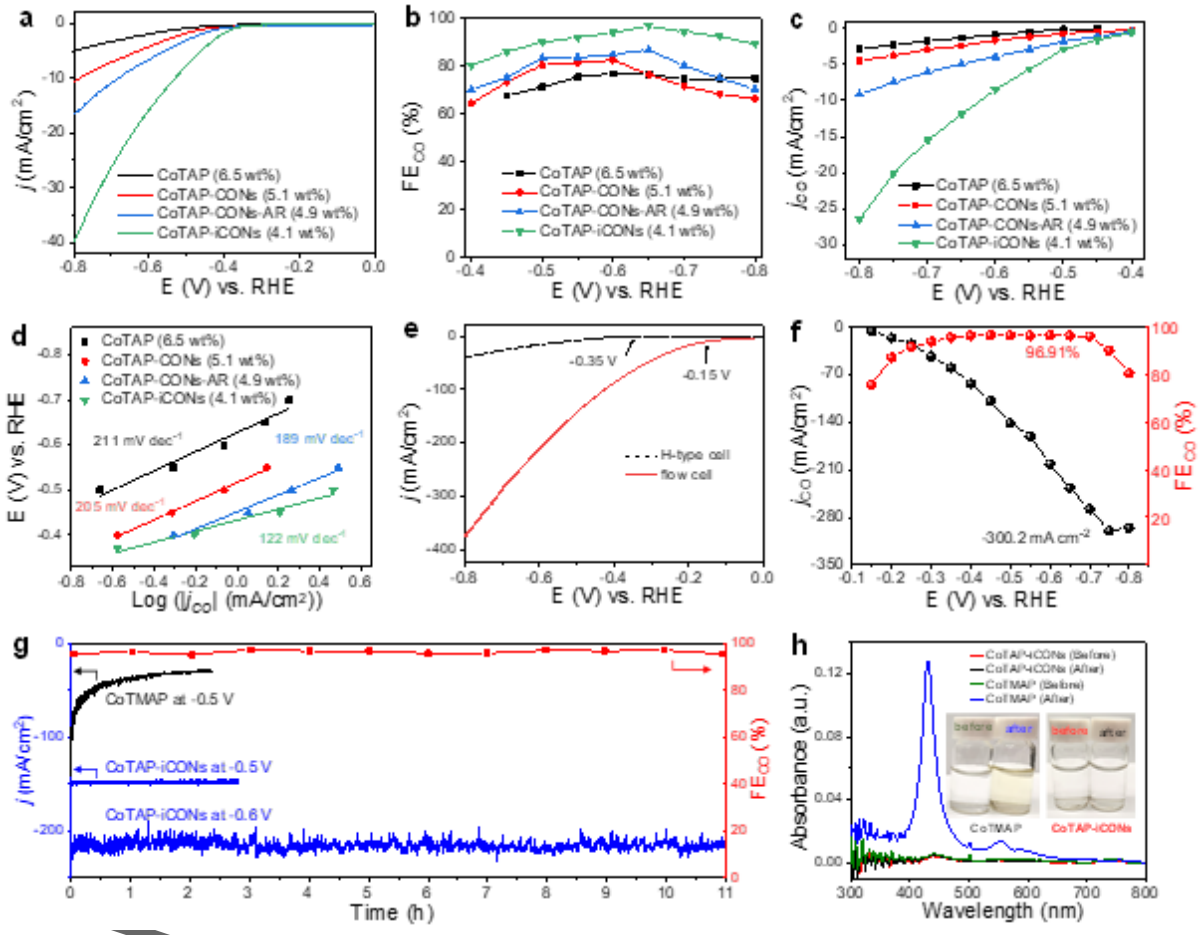

Figure 3. (a) LSV curves in CO_2-saturated 0.5 M $KHCO_3$, (b) Faradaic efficiency measurements, (c) Carbon monoxide partial current density curves and (d) Tafel plots of CoTAP, CoTAP-CONs, CoTAP-CONs-AR, and CoTAP-iCON in a home-made H-cell. The cobalt contents of different samples in (a-d) are all ~6.5 μg cm^{-2}. (e) LSV curves of CoTAP-iCONs in different types of electrolyzers (red line: 1 M KOH in flow cell; black line: 0.5 M $KHCO_3$ in H-cell). (f) Current density and Faradaic efficiency towards CO of CoTAP-iCONs using a flow cell reactor, (g) Chronoamperometry tests of CoTAP-iCONs and CoTMAP at -0.5 V and -0.6 V vs RHE. (h) UV-vis spectra of CoTAP-iCONs and CoTMAP before and after electrolysis. The inserts are the electrolytes before and after electrolysis.

The spectroscopy and microscope data reveal that CoTAP-iCONs adopt an ultrathin nanosheets structure with positively charged ammonium groups. These structural characteristics are conducive to CO_2 electroreduction. For example, the ultrathin structure makes the active sites highly dispersed and accessible. The cationic units could improve the activity and they are stabilized in the framework[27-34]. The CO_2 reduction activities of all samples are first evaluated in a home-made H-type cell. The loading amount of cobalt in different catalysts is the same by controlling the catalyst quantity. As revealed by linear sweep voltammetry (LSV) curves in **Figure 3**a, CoTAP-iCONs deliver a more positive onset potential (-0.35 V) and higher current density in CO_2-saturated 0.5 M $KHCO_3$ electrolyte. It reaches a current density of 40.1 mA cm^{-2} at -0.8 V, which is much higher than that of CoTAP (5.0 mA cm^{-2}), CoTAP-CONs (10.5 mA cm^{-2}), and CoTAP-CONs-AR (16.8 mA cm^{-2}). To get insight into the catalytic selectivity, chronoamperometry experiments are performed at different potentials from -0.4 to -0.8 V (Figure S6a). The primary products detected are only CO and H_2, and no liquid products are generated according to ^{1}H NMR spectroscopy in Figure S7. CoTAP-iCONs achieve the highest carbon monoxide Faradaic efficiency (FE_{CO}) of 96.74% at -0.65 V, whereas CoTAP-CONs and CoTAP-CONs-AR show lower Faradaic efficiency (< 90%) in the whole potential range (Figure 3b), revealing that the ammonium groups play an important role in selective and efficient reduction of CO_2. Figure 3c shows the partial CO current density (j_{CO}): CoTAP-iCONs present a high value of 26.4 mA cm^{-2} at -0.8 V, which increases by ~910% and ~580% compared to that of CoTAP (2.9 mA cm^{-2}) and CoTAP-CONs (4.5 mA cm^{-2}) respectively. This performance is also better than most reported cobalt porphyrin-derived electrocatalysts[9,43,49,66-68] (Table S2). The turnover frequencies (TOFs) for CO generation are calculated by the cobalt amount according to ICP results. The TOF of CoTAP-iCONs is found to be 1.25 s^{-1} at -0.8 V (Figure S6b). To explore the dynamic activity, the Tafel slopes of 211,

205, 189 and 122 mV dec^{-1} are obtained for CoTAP, CoTAP-CONs, CoTAP-CONs-AR, and CoTAP-iCONs (Figure 3d). The Tafel slope of CoTAP-iCONs is close to the theoretical value of a concerted proton-electron transfer rate-determining mechanism, which also indicates the fast electron transfer at the catalyst/electrode interface[69,70]. All these results suggest that the electrostatic repulsion effect makes the positively charged nanosheets uniformly dispersed and the active sites highly exposed. Furthermore, the stability of CoTAP-iCONs for CO_2RR in H-type cell is tested at -0.6 V, and no obvious decays of FE_{CO} or current density are observed in Figure S6c within 8000-s test.

To understand the effect of functional groups in CO_2RR activities, we use DFT calculations to reveal the change of energy barriers in CO_2RR and the competing HER. **Figure 4**a shows the models of CoTAP-CONs, CoTAP-CONs-AR and CoTAP-iCONs, which are constructed from their structural characterizations. The energy barriers for the generation of *COOH (~0.84 eV) in all the samples are higher than those of *CO desorption (~0.1 eV), which suggests that the rate-determining step is the formation of *COOH and is consistent with literature studies[49,67,71,72]. Therefore, a lower energy barrier for the formation of *COOH will be favorable for CO_2RR process. Meanwhile, a higher energy barrier for HER is also conducive as it indicates that the competing side reaction is unfavorable. Figure 4b show that the decoration of quaternary ammonium group results in the reduced energies of *COOH formation from 0.85 eV for CoTAP-CONs and CoTAP-CONs-AR to 0.82 eV for CoTAP-iCONs. Furthermore, a minute increase of *H energy is observed for CoTAP-iCONs (0.747 eV) in comparison to CoTAP-CONs and CoTAP-CONs-AR. These analyses suggest that the quaternary ammonium group can boost the CO_2RR performance by facilitating *COOH formation. However, it should be noted that the calculations only provide perspectives from the catalysts themselves; they do not account for the local pH, solvation effect, diffusional effect, and the electrostatic interactions with additives such

as Nafion, which could change the local environment and impact the catalytic performance. More thorough calculations combined with spectroscopic evidence could help to better understand the effects of ionic groups in CO_2RR.

Due to the limited solubility of CO_2 in an aqueous solution, the current densities in H-type cell are restricted by mass transport[73,74]. Electrocatalytic CO_2RR performances are further evaluated in a flow cell reactor. Previous studies suggested that alkaline electrolytes can lower the CO_2 activation energy barrier and suppress the competing hydrogen evolution reaction[75,76]. Therefore, 1 M KOH is used as the electrolyte in our flow cell configuration, and an anion exchange membrane (AEM) is applied as the separator. As shown in Figure 3e, the onset potential positively shifts to -0.15 V and the current density significantly increases to 375.1 mA cm^{-2} at -0.8 V. CoTAP-iCONs maintain a high selectivity of more than 90% in a wide potential range from -0.25 V to -0.75 V, but decrease to 80.7% at -0.8 V as illustrated by the red line in Figure 3f. The highest partial CO current density of 300.2 mA cm^{-2} is achieved at -0.75 V, and when the applied voltage reaches -0.8 V, the partial current density of CO declines to 296.4 mA cm^{-2}. The decrease of partial current density at higher overpotential might be due to the salt precipitation or dissolution in alkaline solution[73,77]. The detailed current densities measured at different potentials are displayed in Figure S8a.

To further highlight the significance of layered structure, ionic molecular catalysts of cobalt tetra-(4-*N*,*N*,*N*-trimethylanilinium)porphyrin (CoTMAP) is synthesized and investigated in a flow cell electrolyzer for comparison (Figure S9). The current density of CoTMAP is unstable and declines from 114.1 to 30.1 mA cm^{-2} in 8000 s at -0.5 V (Figure 3g). CoTMAP shows obvious catalyst leaching during operation; the catholyte turns yellow (Figure S10) and exhibits an absorption peak at 430 nm (Figure 3h). However, no obvious absorption peak is detected for CoTAP-iCONs after electrolysis (black line).

The cobalt content in the electrolyte is determined by ICP, which shows that 38.4% cobalt is extracted from CoTMAP and the Co content in the catholyte of CoTAP-iCONs is below the detection limit. Thereby, the incorporation of charged cobalt porphyrin units into the extended framework of CoTAP-iCONs efficiently resolves the leaching problem of ionic molecular catalysts.

Considering the sulfonic groups in Nafion structure may act as counter ions to stabilize ionic molecular catalysts[78], the influence of Nafion loading on the stability of CoTMAP is investigated. We vary the Nafion content in catalyst ink to prepare GDEs and keep the catalyst loading constant. In the case of low Nafion content (0.2%), the adhesion between CoTMAP and substrate is weak, therefore CoTMAP gradually detaches from the GDE surface and the current density decays with time (Figure S11b). Besides, the coloration of electrolyte is observed during electrolysis. According to the LSV curves (Figure S11a), CoTMAP shows an initial current density of 232 mA cm^{-2} at -0.8 V, but it decreases to 153 mA cm^{-2} after electrolysis. When the Nafion content is further increased to 6%, the current density at each potential slightly decreases (Figure S11e), and CoTMAP presents relatively stable CO_2RR activity. However, the current density of CoTMAP with high Nafion content (6%) is generally lower than that of low Nafion content (0.2%). This may be attributed to the Nafion agglomeration, which wraps the catalyst surface and increases charge transfer resisitance[79-81]. To confirm this, impedance spectroscopy tests are conducted. As revealed by the Nyquist plots (Figure S11c,f), CoTMAP with high Nafion content (6%) shows larger charge transfer resistance (4.34 Ω) than that with low content (1.41 Ω) at -0.4 V. Therefore, the addition of Nafion ionomer helps the attachment of CoTMAP to GDE substrate, but excessive Nafion amount will degrade catalyst performance.

We further compare the performance of CoTMAP and CoTAP-iCONs with different loadings of 0.5, 1, and 2 mg/cm^2 (Figure S12-13). Due to the weak interaction between CoTMAP and GDE, the current density of CoTMAP decreases during electrolysis when the catalyst loading is 0.5 and 1 mg cm^{-2}. Further increasing catalyst loading to 2 mg cm^{-2} enhances the activity and slows down the decay of current density (Figure S12). In contrast, CoTAP-iCONs display stable current densities at different loadings. The current density of CoTAP-iCONs increases from 230 to 290 mA cm^{-2} at -0.7 V when the catalyst loading increases from 0.5 to 2 mg cm^{-2} (Figure S13d,f). As summarized in Figure S14, both CoTMAP and CoTAP-iCONs can deliver a current density beyond 100 mA cm^{-2}. CoTAP-iCONs in general show higher current densities and better stability than the molecular counterpart, which further corroborates the effectiveness in confining charged molecules in layered structure.

Long-term stability of CoTAP-iCONs in flow cell is investigated at -0.6 V vs RHE in 1 M KOH, the partial current density of CO is maintained around 201.4 mA cm^{-2} for 11 h, and the carbon monoxide selectivity remains above 95% during the whole process (Figure 3g). To further investigate the stability, the CoTAP-iCONs after the long-term flow cell operated at -0.6 V vs RHE is characterized by FTIR, UV-vis, XPS and ICP characterizations. The recovered sample of CoTAP-iCONs in FTIR exhibits characteristic peaks similar to those of the original (Figure S15a). Some additional peaks corresponding to the Nafion at 950-1300 cm^{-1} also appear. Nonetheless, the peaks at 1700-1400 cm^{-1} and 950-400 cm^{-1}, which are attributed to the vibration of porphyrin and benzene rings, are almost identical after electrolysis[82,83]. In addition, the vibration of -N^+-$(CH_3)_2$- groups at 956 and 1480 cm^{-1}, as well as the Co-N stretching at 1005 cm^{-1}, also retains after electrolysis. The optical prosperity of CoTAP-iCONs after electrolysis is also characterized using UV-vis spectroscopy. HTAP-iCONs are prepared for comparison under the same synthetic conditions with CoTAP-iCONs except replacing

CoTAP with 5,10,15,20-tetrakis(4-aminophenyl)-21H,23H-porphine (HTAP). HTAP-iCONs show a Soret band at 435.8 nm, whereas the CoTAP-iCONs show a blue shift at 428 nm due to the metalation effect[84,85]. Compared with the raw CoTAP-iCONs, no obvious shift are observed after electrolysis. XPS analysis is applied to study the chemical state and bonding environment of post-electrolysis sample. The Co 2p peaks reveal no apparent change after electrolysis, indicating the Co metal center can maintain its primary valence state of +2. From the TEM image in Figure S16c,d, the morphology of CoTAP-iCON has no significant change and no obvious aggregation of metal nanoparticles are observed. The amount of cobalt in the electrolyte is also measured by ICP, which shows a negligible content of Co. The above post-analytic characterizations suggest the integrity of CoTAP-iCONs is preserved and no apparent amount of cobalt is leached after the long-term electrolysis.

The electrolyte is replaced with 1 M $KHCO_3$ in flow cell to investigate the CO_2RR performance of CoTAP-iCONs in the neutral environment (Figure S17). As shown in Figure S17a, CoTAP-iCONs exhibit an onset potential of -0.33 V and reaches a current density of 207.2 mA cm^{-2} at -0.8 V. The selectivity of CO under different potentials within 30 min are displayed in Figure S17b. CoTAP-iCONs present high FE_{CO} of over 90% in the applied potential range between -0.4 V and -0.8 V, and the total current density is found to increase from 16 to 186.5 mA cm^{-2}. In addition, the stability test of CoTAP-iCONs in neutral medium is operated at -0.8 V for 5 h. The FE_{CO} can be maintained higher than 92% and the CO partial current density remains at about 175 mA cm^{-2} (Figure S17c). Finally, the performance comparison of recent electrocatalysts for CO_2-to-CO conversion on gas diffusion electrodes is shown in Table S3. CoTAP-iCONs exhibit high activity and selectivity and are even comparable to noble metal catalysts[28,86-89].

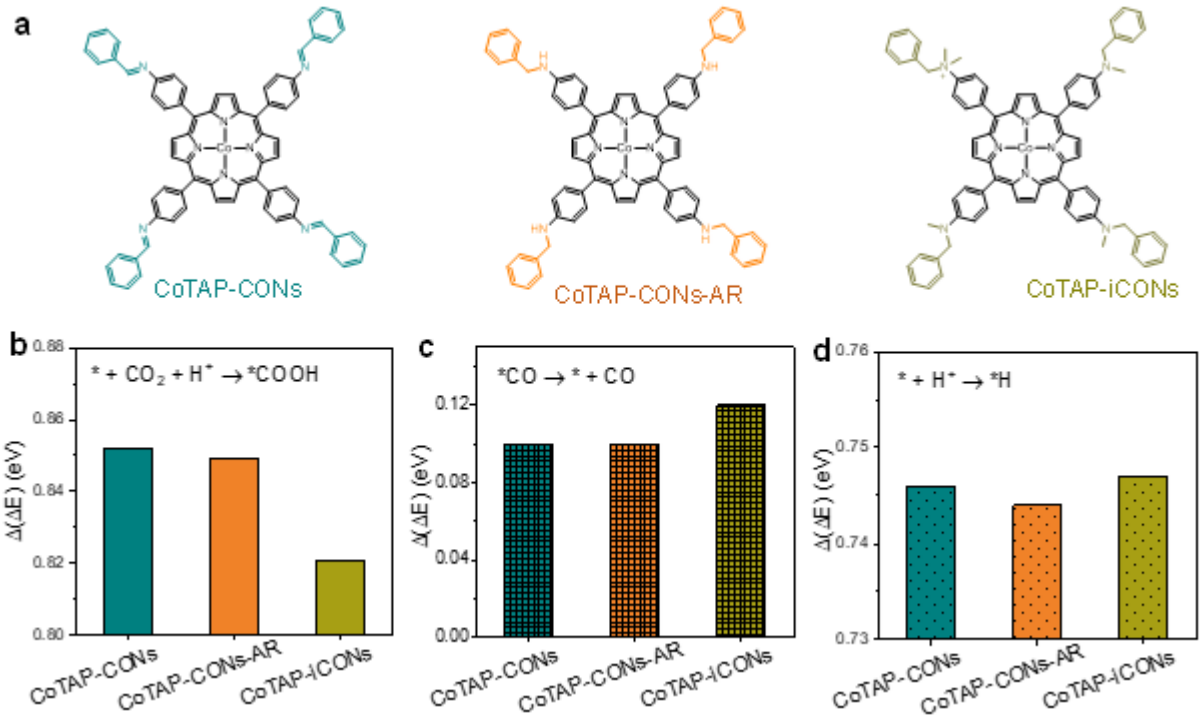

Figure 4. (a) Structures of CoTAP-CONs, CoTAP-CONs-AR and CoTAP-iCONs. Energy for the formation of *COOH (b), *CO (c) and *H (d) adsorbed on CoTAP-CONs, CoTAP-CONs-AR and CoTAP-iCONs.

As mentioned above, CoTAP-iCONs exhibit low onset potential and high current density in a flow cell reactor, possessing a great potential as the cathode for photovoltaic-electrochemical (PV-EC) systems. We choose Fe/Ni foam as the anode (See Supporting Information for preparation) and two commercial GaInP/GaInAs/Ge triple-junction solar cells with an area of 1 cm × 1 cm connected in parallel as the power source. The integrated PV-EC system is designed and depicted in **Figure 5**a (photography in Figure S18). The LSV curves of cathodic and anodic reaction is shown in Figure 5b, and the current values measured at different full CO_2RR/OER cell potentials are shown in Figure 5c (black curve; detailed chronoamperometry data are shown in Figure S20). The *I-V* characteristic curve of the complete photovoltaic module is also shown in Figure 5c, which attains an open-circuit

voltage (V_{oc}) of 2.58 V and a short-circuit current (J_{sc}) of 22.25 mA under 1 sun illumination. When using the photovoltaic module to drive electrocatalytic flow cell, the operating voltage and current can be derived from the intersection point of two curves in Figure 5c, which are determined to be 1.848 V and 21.87 mA, respectively. The current of PV-EC system is measured over 12 hours (Figure 5d), which shows the stable solar-to-carbon monoxide conversion with an efficiency of ~13.89%. During the long-term solar-driven CO_2RR/OER electrolysis, the actual working voltage stays at 1.88 V (Figure S21), which is close to the theoretic operating voltage of 1.848 V (Figure 5c).

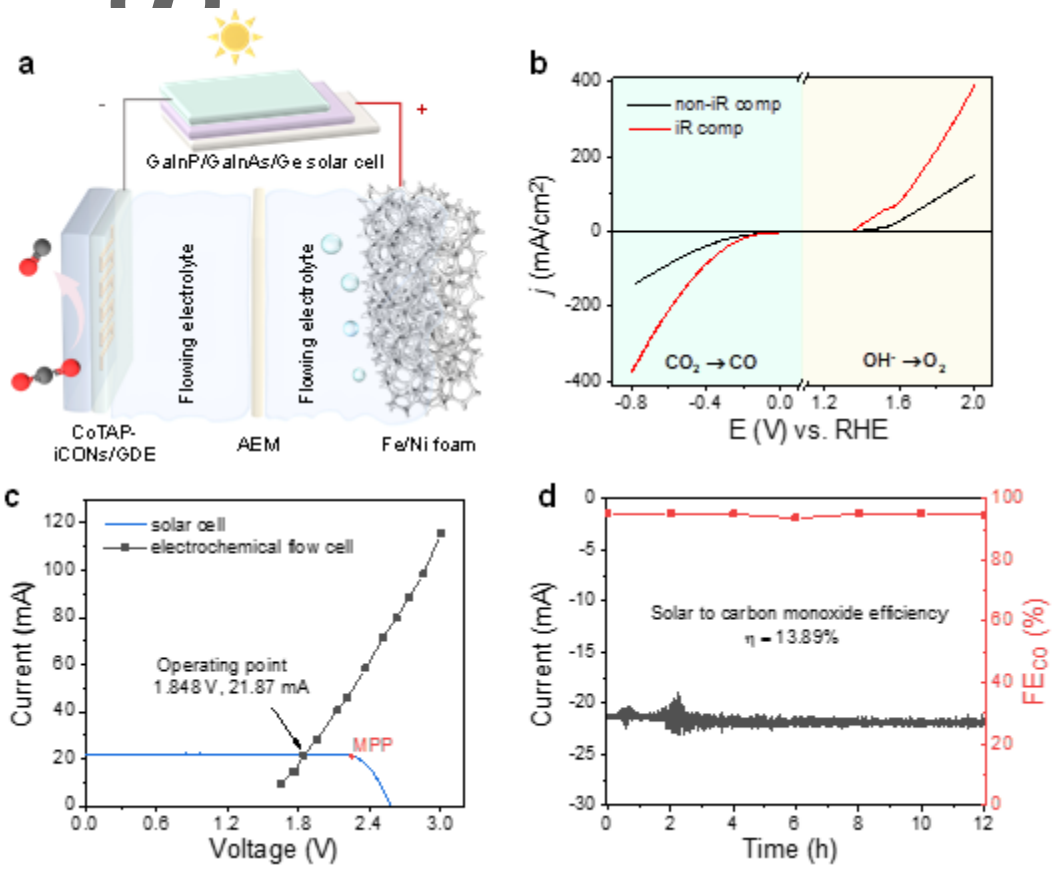

Figure 5. (a) Schematic of the solar-driven CO_2 reduction device combining photovoltaics with an electrochemical flow cell. (b) LSV curves of CO_2RR/OER full cell with and without iR compensations

(cathode: CoTAP-iCONs; catholyte: 1 M KOH; anode: Fe/Ni foam; anolyte: 1 M KOH). (c) *I-V* curve of GaInP/GaInAs/Ge triple-junction solar cell under 1 sun illumination and measured operating currents at different full cell potentials without iR compensation. (d) Current density and solar-to-CO conversion efficiency of the PV-EC device during 12-h stability test.

Even though our performance is higher than some reported works[90-93] (Table S4), the conversion efficiency is limited by the solar cell performance. As shown in Figure 5c, the crossing point falls far from the maximum power point (MPP) of photovoltaic device, leading to underdeveloped energy conversion. Therefore, the development of more efficient solar cells with higher J_{sc} to power our electrocatalytic flow cell can improve the solar energy conversion efficiency. Moreover, the performance can be further improved by lowering the energy losses due to resistance. Figure 5b shows the LSV curves of two individual half-cells with and without iR compensation. The ohmic drop of solution resistance and membrane resistance inevitably causes energy loss of full cell[94-96]. A higher concentration of electrolyte solutions and a faster diffusion rate of ions across the exchange membrane are conducive to minimizing the full cell resistance.

3. Conclusion

We have prepared atomically thin, positively charged, cobalt porphyrin-based covalent organic nanosheets for high-performance CO_2 reduction reaction. It is a new example of ionic structure that could be applicable in general for heterogenizing ionic molecules[28,29] with high stability, expanding the library of stable ionic electrocatalysts[36,78]. There are two key roles for the quaternary ammonium groups. One is the structural effect: the steric hindrance and electrostatic repulsion of methylated ammonium groups in the skeleton effectively reduce the thickness of CoTAP-iCONs. This

ultrathin structure highly exposes the cobalt active sites and facilitates the transfer of electrons from electrode to CoTAP-iCONs. The other is a comprehensive result of inductive effect and electrostatic effect[22,24,25]. The electron-withdrawing effect of quaternary ammonium groups in the framework reduces electron densities of metal centers; these cationic groups could electrostatically stabilize the negatively charged $CO_2^{\bullet-}$ intermediate, and repulse the hydronium for HER. These are witnessed by a significantly improved CO selectivity and partial current density of 26.4 mA cm^{-2} at -0.8 V for CoTAP-iCONs in an H-type cell. The carbon monoxide partial current density of CoTAP-iCONs could reach up to 300.2 mA cm^{-2} at -0.75 V in a flow cell configuration. Moreover, CoTAP-iCONs exhibit good stability with a total current density of 212 mA cm^{-2} and a CO Faradaic efficiency over 95% at -0.6 V for 11 h. Finally, we demonstrate a solar-driven CO_2-to-CO conversion system by integrating a CoTAP-iCONs electrocatalytic flow cell and commercial photovoltaic cells. Our PV-EC system has a 13.89% solar-to-CO conversion efficiency over 12-h continuous process. This work offers a strategy for stabilizing ionic molecular catalysts and designing atomically thin covalent organic nanosheets. Admittedly, the preparation of iCONs is more sophisticated than the direct use of ionic molecular catalysts, yet it is effective and applicable to achieve both high stability and activity for ionic catalysts with high water solubility.

Supporting Information

Supporting Information is available from the Wiley Online Library or from the author.

Acknowledgements

R.Y. thanks the support from the Guangdong Basic and Applied Basic Research Fund (No. 2022A1515011333), the Science, Technology and Innovation Commission of Shenzhen under Shenzhen Virtual University Park Special Fund (No. 2021Szvup129), the Hong Kong Research Grant Council under Early Career Scheme (No. 21300620) and General Research Fund (No. 11307120), Shenzhen-Hong Kong-Macau Science and Technology Grant [type C; SGDX2020110309300301] from the Science, Technology and Innovation Commission of Shenzhen Municipality, and State Key Laboratory of Marine Pollution Seed Collaborative Research Fund (SKLMP/IRF/0029).

Conflict of interest

The authors declare no conflict of interest.

References

[1] X. Zhang, Y. Wang, M. Gu, M. Wang, Z. Zhang, W. Pan, Z. Jiang, H. Zheng, M. Lucero, H. Wang, G. E. Sterbinsky, Q. Ma, Y. G. Wang, Z. Feng, J. Li, H. Dai, Y. Liang, *Nat. Energy* **2020**, *5*, 684.

[2] D. Gao, T. Liu, G. Wang, X. Bao, *ACS Energy Lett.* **2021**, *6*, 713.

[3] A. S. Varela, W. Ju, P. Strasser, *Adv. Energy Mater.* **2018**, *8*, 1703614.

[4] Z. Zhang, J. Xiao, X. J. Chen, S. Yu, L. Yu, R. Si, Y. Wang, S. Wang, X. Meng, Y. Wang, Z. Q. Tian, D. Deng, *Angew. Chem.* **2018**, *57*, 16339.

[5] X. Zhang, Z. Wu, X. Zhang, L. Li, Y. Li, H. Xu, X. Li, X. Yu, Z. Zhang, Y. Liang, H. Wang, *Nat. Commun.* **2017**, *8*, 14675.

[6] Y. Zhong, S. Wang, M. Li, J. Ma, S. Song, A. Kumar, H. Duan, Y. Kuang, X. Sun, *Mater. Today Phys.* **2021**, *18*, 100354.

[7] Y. R. Wang, M. Liu, G. K. Gao, Y. L. Yang, R. X. Yang, H. M. Ding, Y. Chen, S. L. Li, Y. Q. Lan, *Angew. Chem.* **2021**, *60*, 21952.

[8] F. Lv, N. Han, Y. Qiu, X. Liu, J. Luo, Y. Li, *Coord. Chem. Rev.* **2020**, *422*, 213435.

[9] Y.-R. Wang, Q. Huang, C.-T. He, Y. Chen, J. Liu, F.-C. Shen, Y.-Q. Lan, *Nat. Commun.* **2018**, *9*, 4466.

[10] H. Zhong, M. Ghorbani-Asl, K. H. Ly, J. Zhang, J. Ge, M. Wang, Z. Liao, D. Makarov, E. Zschech, E. Brunner, I. M. Weidinger, J. Zhang, A. V. Krasheninnikov, S. Kaskel, R. Dong, X. Feng, *Nat. Commun.* **2020**, *11*, 1409.

[11] J. D. Froehlich, C. P. Kubiak, *Inorg. Chem.* **2012**, *51*, 3932.

[12] C. Costentin, M. Robert, J. M. Savéant, *Chem. Rev.* **2008**, *108*, 2348.

[13] K. HIRATSUKA, K. TAKAHASHI, H. SASAKI, S. TOSHIMA, *Chem. Lett.* **1977**, *6*, 1137.

[14] C. Costentin, J. M. Savéant, *Curr. Opin. Electrochem.* **2019**, *15*, 58.

[15] R. Francke, B. Schille, M. Roemelt, *Chem. Rev.* **2018**, *118*, 4631.

[16] E. Boutin, L. Merakeb, B. Ma, B. Boudy, M. Wang, J. Bonin, E. Anxolabéhère-Mallart, M. Robert, *Chem. Soc. Rev.* **2020**, *49*, 5772.

[17] F. Franco, C. Rettenmaier, H. S. Jeon, B. Roldan Cuenya, *Chem. Soc. Rev.* **2020**, *49*, 6884.

[18] D. Behar, T. Dhanasekaran, P. Neta, C. M. Hosten, D. Ejeh, P. Hambright, E. Fujita, *J. Phys. Chem. A* **1998**, *102*, 2870.

[19] B. J. Fisher, R. Eisenberg, *J. Am. Chem. Soc.* **1980**, *102*, 7361.

[20] C. Costentin, G. Passard, M. Robert, J. M. Savéant, *Proc. Natl. Acad. Sci. U. S. A.* **2014**, *111*, 14990.

[21] I. Azcarate, C. Costentin, M. Robert, J. M. Savéant, *J. Phys. Chem. C* **2016**, *120*, 28951.

[22] I. Azcarate, C. Costentin, M. Robert, J. M. Savéant, *J. Am. Chem. Soc.* **2016**, *138*, 16639.

[23] C. Costentin, M. Robert, J. M. Savéant, A. Tatin, *Proc. Natl. Acad. Sci. U. S. A.* **2015**, *112*, 6882.

[24] A. Tatin, C. Comminges, B. Kokoh, C. Costentin, M. Robert, J. M. Savéant, *Proc. Natl. Acad. Sci. U. S. A.* **2016**, *113*, 5526.

[25] C. Costentin, M. Robert, J. M. Savéant, *Curr. Opin. Electrochem.* **2017**, *2*, 26.

[26] W. Nie, D. E. Tarnopol, C. C. L. McCrory, *J. Am. Chem. Soc.* **2021**, *143*, 3764.

[27] J. Choi, P. Wagner, R. Jalili, J. Kim, D. R. MacFarlane, G. G. Wallace, D. L. Officer, *Adv. Energy Mater.* **2018**, *8*, 1801280.

[28] J. Su, J. J. Zhang, J. Chen, Y. Song, L. Huang, M. Zhu, B. I. Yakobson, B. Z. Tang, R. Ye, *Energy Environ. Sci.* **2021**, *14*, 483.

[29] M. Zhu, D. T. Yang, R. Ye, J. Zeng, N. Corbin, K. Manthiram, *Catal. Sci. Technol.* **2019**, *9*, 974.

[30] J. Choi, P. Wagner, S. Gambhir, R. Jalili, D. R. Macfarlane, G. G. Wallace, D. L. Officer, *ACS Energy Lett.* **2019**, *4*, 666.

[31] M. Zhu, J. Chen, L. Huang, R. Ye, J. Xu, Y. F. Han, *Angew. Chem.* **2019**, *58*, 6595.

[32] L. Sun, V. Reddu, A. C. Fisher, X. Wang, *Energy Environ. Sci.* **2020**, *13*, 374.

[33] D. D. Ma, S. G. Han, C. Cao, W. Wei, X. Li, B. Chen, X. T. Wu, Q. L. Zhu, *Energy Environ. Sci.* **2021**, *14*, 1544.

[34] S. A. Yao, R. E. Ruther, L. Zhang, R. A. Franking, R. J. Hamers, J. F. Berry, *J. Am. Chem. Soc.* **2012**, *134*, 15632.

[35] X. M. Hu, M. H. Rønne, S. U. Pedersen, T. Skrydstrup, K. Daasbjerg, *Angew. Chem.* **2017**, *56*, 6468.

[36] M. Wang, K. Torbensen, D. Salvatore, S. Ren, D. Joulié, F. Dumoulin, D. Mendoza, B. Lassalle-Kaiser, U. Işci, C. P. Berlinguette, M. Robert, *Nat. Commun.* **2019**, *10*, 3602.

[37] J. Choi, J. Kim, P. Wagner, S. Gambhir, R. Jalili, S. Byun, S. Sayyar, Y. M. Lee, D. R. MacFarlane, G. G. Wallace, D. L. Officer, *Energy Environ. Sci.* **2019**, *12*, 747.

[38] Y. Wang, J. Chen, G. Wang, Y. Li, Z. Wen, *Angew. Chem.* **2018**, *57*, 13120.

[39] P. Su, K. Iwase, T. Harada, K. Kamiya, S. Nakanishi, *Chem. Sci.* **2018**, *9*, 3941.

[40] C. Lu, J. Yang, S. Wei, S. Bi, Y. Xia, M. Chen, Y. Hou, M. Qiu, C. Yuan, Y. Su, F. Zhang, H. Liang, X. Zhuang, *Adv. Funct. Mater.* **2019**, *29*, 1806884.

[41] B. Han, X. Ding, B. Yu, H. Wu, W. Zhou, W. Liu, C. Wei, B. Chen, D. Qi, H. Wang, K. Wang, Y. Chen, B. Chen, J. Jiang, *J. Am. Chem. Soc.* **2021**, *143*, 7104.

[42] C. S. Diercks, S. Lin, N. Kornienko, E. A. Kapustin, E. M. Nichols, C. Zhu, Y. Zhao, C. J. Chang, O. M. Yaghi, *J. Am. Chem. Soc.* **2018**, *140*, 1116.

[43] S. Lin, C. S. Diercks, Y. B. Zhang, N. Kornienko, E. M. Nichols, Y. Zhao, A. R. Paris, D. Kim, P. Yang, O. M. Yaghi, C. J. Chang, *Science* **2015**, *349*, 1208.

[44] J. J. Leung, J. A. Vigil, J. Warnan, E. Edwardes Moore, E. Reisner, *Angew. Chem.* **2019**, *131*, 7779.

[45] J. K. Tang, C. Y. Zhu, T. W. Jiang, L. Wei, H. Wang, K. Yu, C. L. Yang, Y. B. Zhang, C. Chen, Z. T. Li, D. W. Zhang, L. M. Zhang, *J. Mater. Chem. A* **2020**, *8*, 18677.

[46] S. Wei, H. Zou, W. Rong, F. Zhang, Y. Ji, L. Le Duan, *Appl. Catal. B Environ.* **2021**, *284*, 119739.

[47] D. Yang, S. Zuo, H. Yang, Y. Zhou, X. Wang, *Angew. Chem.* **2020**, *59*, 18954.

[48] M. Wang, H. Shi, P. Zhang, Z. Liao, M. Wang, H. Zhong, F. Schwotzer, A. S. Nia, E. Zschech, S. Zhou, S. Kaskel, R. Dong, X. Feng, *Adv. Funct. Mater.* **2020**, *30*, 2002664.

[49] J. Han, P. An, S. Liu, X. Zhang, D. Wang, Y. Yuan, J. Guo, X. Qiu, K. Hou, L. Shi, Y. Zhang, S. Zhao, C. Long, Z. Tang, *Angew. Chem.* **2019**, *58*, 12711.

[50] S. Zhao, Y. Wang, J. Dong, C. T. He, H. Yin, P. An, K. Zhao, X. Zhang, C. Gao, L. Zhang, J. Lv, J. Wang, J. Zhang, A. M. Khattak, N. A. Khan, Z. Wei, J. Zhang, S. Liu, H. Zhao, Z. Tang, *Nat. Energy* **2016**, *1*, 1.

[51] W. Wang, W. Zhao, H. Xu, S. Liu, W. Huang, Q. Zhao, *Coord. Chem. Rev.* **2021**, *429*, 213616.

[52] Y. Peng, Y. Huang, Y. Zhu, B. Chen, L. Wang, Z. Lai, Z. Zhang, M. Zhao, C. Tan, N. Yang, F. Shao, Y. Han, H. Zhang, *J. Am. Chem. Soc.* **2017**, *139*, 8698.

[53] M. A. Khayum, S. Kandambeth, S. Mitra, S. B. Nair, A. Das, S. S. Nagane, R. Mukherjee, R. Banerjee, *Angew. Chem.* **2016**, *128*, 15833.

[54] A. Mal, S. Vijayakumar, R. K. Mishra, J. Jacob, R. S. Pillai, B. S. Dileep Kumar, A. Ajayaghosh, *Angew. Chem.* **2020**, *132*, 8791.

[55] F. Meng, S. Bi, Z. Sun, B. Jiang, D. Wu, J. Chen, F. Zhang, *Angew. Chem.* **2021**, *133*, 13726.

[56] L. Wang, C. Zeng, H. Xu, P. Yin, D. Chen, J. Deng, M. Li, N. Zheng, C. Gu, Y. Ma, *Chem. Sci.* **2019**, *10*, 1023.

[57] K. Li, N. K. Wong, M. J. Strauss, A. M. Evans, M. Matsumoto, W. R. Dichtel, A. Adronov, *J. Am. Chem. Soc.* **2021**, *143*, 649.

[58] W. Liu, X. Li, C. Wang, H. Pan, W. Liu, K. Wang, Q. Zeng, R. Wang, J. Jiang, *J. Am. Chem. Soc.* **2019**, *141*, 17431.

[59] H. Sahabudeen, H. Qi, B. A. Glatz, D. Tranca, R. Dong, Y. Hou, T. Zhang, C. Kuttner, T. Lehnert, G. Seifert, U. Kaiser, A. Fery, Z. Zheng, X. Feng, *Nat. Commun.* **2016**, *7*, 13461.

[60] Y. Yusran, H. Li, X. Guan, D. Li, L. Tang, M. Xue, Z. Zhuang, Y. Yan, V. Valtchev, S. Qiu, Q. Fang, *Adv. Mater.* **2020**, *32*, 1907289.

[61] S. Jhulki, J. Kim, I. C. Hwang, G. Haider, J. Park, J. Y. Park, Y. Lee, W. Hwang, A. A. Dar, B. Dhara, S. H. Lee, J. Kim, J. Y. Koo, M. H. Jo, C. C. Hwang, Y. H. Jung, Y. Park, M. Kataria, Y. F. Chen, S. H. Jhi, M. H. Baik, K. Baek, K. Kim, *Chem* **2020**, *6*, 2035.

[62] Z.-J. Yin, S.-Y. Jiang, N. Liu, Q.-Y. Qi, Z.-Q. Wu, T.-G. Zhan, X. Zhao, *CCS Chem.* **2021**, 614.

[63] H.-J. Zhu, M. Lu, Y.-R. Wang, S.-J. Yao, M. Zhang, Y.-H. Kan, J. Liu, Y. Chen, S.-L. Li, Y.-Q. Lan, *Nat. Commun.* **2020**, *11*, 497.

[64] B. P. Biswal, S. Valligatla, M. Wang, T. Banerjee, N. A. Saad, B. M. K. Mariserla, N. Chandrasekhar, D. Becker, M. Addicoat, I. Senkovska, R. Berger, D. N. Rao, S. Kaskel, X. Feng, *Angew. Chem.* **2019**, *131*, 6970.

[65] S. Yang, Y. Yu, M. Dou, Z. Zhang, F. Wang, *J. Am. Chem. Soc.* **2020**, *142*, 17524.

[66] S. Feng, W. Zheng, J. Zhu, Z. Li, B. Yang, Z. Wen, J. Lu, L. Lei, S. Wang, Y. Hou, *Appl. Catal. B Environ.* **2020**, *270*, 118908.

[67] Q. Wu, R. K. Xie, M. J. Mao, G. L. Chai, J. D. Yi, S. S. Zhao, Y. B. Huang, R. Cao, *ACS Energy Lett.* **2020**, *5*, 1005.

[68] X. Da Zhang, S. Z. Hou, J. X. Wu, Z. Y. Gu, *Chem. - A Eur. J.* **2020**, *26*, 1604.

[69] M. Zhu, R. Ye, K. Jin, N. Lazouski, K. Manthiram, *ACS Energy Lett.* **2018**, *3*, 1381.

[70] N. Han, Y. Wang, L. Ma, J. Wen, J. Li, H. Zheng, K. Nie, X. Wang, F. Zhao, Y. Li, J. Fan, J. Zhong, T. Wu, D. J. Miller, J. Lu, S. T. Lee, Y. Li, *Chem* **2017**, *3*, 652.

[71] Z. Meng, J. Luo, W. Li, K. A. Mirica, *J. Am. Chem. Soc.* **2020**, *142*, 21656.

[72] Sun L, Huang Z, Reddu V, T. Su, A.C. Fisher, X. Wang, *Angew. Chem.* **2020**, *132*, 17252.

[73] H. Rabiee, L. Ge, X. Zhang, S. Hu, M. Li, Z. Yuan, *Energy Environ. Sci.* **2021**, *14*, 1959.

[74] P. Deng, F. Yang, Z. Wang, S. Chen, Y. Zhou, S. Zaman, B. Y. Xia, *Angew. Chem.* **2020**, *59*, 10807.

[75] C. Cao, D. Ma, J. Gu, X. Xie, G. Zeng, X. Li, S. Han, Q. Zhu, X. Wu, Q. Xu, *Angew. Chem.* **2020**, *132*, 15124.

[76] N. Han, P. Ding, L. He, Y. Li, Y. Li, *Adv. Energy Mater.* **2020**, *10*, 1902338.

[77] K. Yang, R. Kas, W. A. Smith, T. Burdyny, *ACS Energy Lett.* **2021**, *6*, 33.

[78] K. Torbensen, C. Han, B. Boudy, N. von Wolff, C. Bertail, W. Braun, M. Robert, *Chem. - A Eur. J.* **2020**, *26*, 3034.

[79] H. Pan, C. J. Barile, *Energy Environ. Sci.* **2020**, *13*, 3567.

[80] E. Antolini, L. Giorgi, A. Pozio, E. Passalacqua, *J. Power Sources* **1999**, *77*, 136.

[81] G. Li, Y. Liu, Q. Zhang, Q. Hu, W. Guo, X. Cao, Y. Dou, L. Cheng, Y. Song, J. Su, L. Huang, R. Ye, *J. Mater. Chem. A* **2022**, DOI 10.1039/d2ta02086f.

[82] X. Cui, Y. Li, Y. Li, B. Qiu, Q. Duan, *Dye. Pigment.* **2019**, *164*, 237.

[83] X. Zhang, H. Liu, J. Qin, H. Han, C. Qiu, S. Zhang, X. Hao, W. Liu, Y. Song, *Chem. Commun.* **2019**, *55*, 5659.

[84] Q. Zuo, G. Cheng, W. Luo, *Dalt. Trans.* **2017**, *46*, 9344.

[85] G. Huang, L. Q. Mo, Y. X. Wei, H. Zhou, Y. A. Guo, S. J. Wei, *Catalysts* **2018**, *8*, 199.

[86] M. Abdinejad, C. Dao, X. an Zhang, H. B. Kraatz, *J. Energy Chem.* **2021**, *58*, 162.

[87] H. Xiang, S. Rasul, B. Hou, J. Portoles, P. Cumpson, E. H. Yu, *ACS Appl. Mater. Interfaces* **2020**, *12*, 601.

[88] S. Ren, D. Joulié, D. Salvatore, K. Torbensen, M. Wang, M. Robert, C. P. Berlinguette, *Science* **2019**, *365*, 367.

[89] R. Shi, J. Guo, X. Zhang, G. I. N. Waterhouse, Z. Han, Y. Zhao, L. Shang, C. Zhou, L. Jiang, T. Zhang, *Nat. Commun.* **2020**, *11*, 3028.

[90] L. Q. Zhou, C. Ling, H. Zhou, X. Wang, J. Liao, G. K. Reddy, L. Deng, T. C. Peck, R. Zhang, M. S. Whittingham, C. Wang, C. W. Chu, Y. Yao, H. Jia, *Nat. Commun.* **2019**, *10*, 4081.

[91] Y. Mi, Y. Qiu, Y. Liu, X. Peng, M. Hu, S. Zhao, H. Cao, L. Zhuo, H. Li, J. Ren, X. Liu, J. Luo, *Adv. Funct. Mater.* **2020**, *30*, 2003438.

[92] M. Schreier, L. Curvat, F. Giordano, L. Steier, A. Abate, S. M. Zakeeruddin, J. Luo, M. T. Mayer, M. Grätzel, *Nat. Commun.* **2015**, *6*, 7326.

[93] M. Schreier, F. Héroguel, L. Steier, S. Ahmad, J. S. Luterbacher, M. T. Mayer, J. Luo, M. Grätzel, *Nat. Energy* **2017**, *2*, 17087.

[94] E. A. Hernández-Pagán, N. M. Vargas-Barbosa, T. Wang, Y. Zhao, E. S. Smotkin, T. E. Mallouk, *Energy Environ. Sci.* **2012**, *5*, 7582.

[95] T. N. Huan, D. A. Dalla Corte, S. Lamaison, D. Karapinar, L. Lutz, N. Menguy, M. Foldyna, S. H. Turren-Cruz, A. Hagfeldt, F. Bella, M. Fontecave, V. Mougel, *Proc. Natl. Acad. Sci. U. S. A.* **2019**, *116*, 9735.

[96] C. E. Creissen, M. Fontecave, *Adv. Energy Mater.* **2020**, *11*, *2002652*.

ToC figure ((Please choose one size: 55 mm broad × 50 mm high **or** 110 mm broad × 20 mm high. Please do not use any other dimensions))

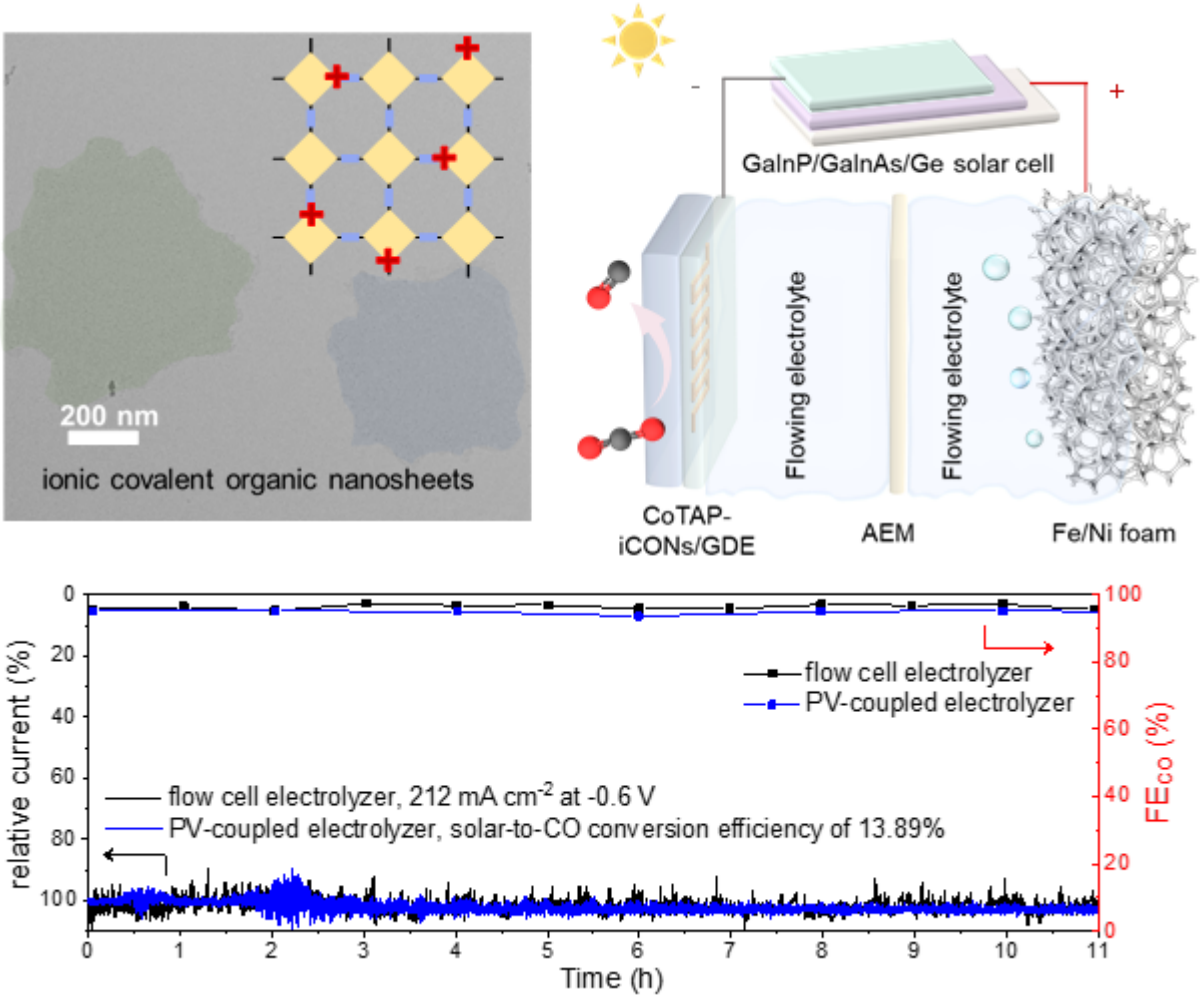

The methylation of cobalt porphyrin-based covalent organic nanosheets successfully introduces cationic quaternary ammonium groups into the framework, and resolves the common leaching problem of ionic molecular catalysts. The steric hindrance and electrostatic repulsion effect of ammonium groups contribute to the formation of monolayer nanosheets and the exposure of active sites. Meanwhile, the quaternary ammonium cations in the skeleton decrease the energy barrier for the formation of *COOH and facilitate electrocatalytic CO_2 reduction to CO.